Tectonomagmatic Setting and Cu-Ni Mineralization Potential of the Gayahedonggou Complex, Northern Qinghai–Tibetan Plateau, China

Namkha Norbu [1,2], Jinchao Li [3,*], Yuegao Liu [4,*], Qunzi Jia [3] and Huilei Kong [3]

1   School of Land Engineering, Chang'an University, Xi'an 710064, China; 2016027001@chd.edu.cn
2   Shaanxi Provincial Land Engineering Construction Group, Xi'an 710075, China
3   Xi'an Center of China Geological Survey, Xi'an 710054, China; xajqunzi@126.com (Q.J.);
    konghuilei2008@126.com (H.K.)
4   CAS Key Laboratory for Experimental Study under Deep-sea Extreme Conditions,
    Institute of Deep-sea Science and Engineering, Chinese Academy of Sciences, Sanya 572000, China
*   Correspondence: lijinchao0313@163.com (J.L.); liuyg@idsse.ac.cn (Y.L.)

check for
updates

Abstract: The Gayahedonggou magmatic Cu-Ni sulfide deposit was recently discovered in the East Kunlun orogenic belt (Northern Tibetan Plateau, China). The mineralization in this region is associated with mafic–ultramafic intrusions. To date, the formation age and metallogenic model of these ore-bearing intrusions have not been studied systematically. In this paper, the petrology, zircon U-Pb chronology, and geochemistry of ore-bearing wehrlite and quartz diorite are investigated. The results show that the zircon U-Pb isotopic age of wehrlite is 419.9 ± 1.5 Ma with an average $\varepsilon Hf(t)$ value of 3.0, indicating that wehrlite originated from a depleted mantle or the asthenosphere. The $(La/Yb)_N$, $(La/Sm)_N$, $(Gd/Yb)_N$, Nb/U, and Ce/Pb ratios of wehrlite are between 3.01–7.14, 1.69–3.91, 1.36–1.51, 2.07–2.93, and 0.55–1.42, respectively, indicating that the parent magma of the wehrlite had been contaminated by the upper crust. The zircon U-Pb isotopic age of quartz diorite is 410.2 ± 3.5 Ma with an average $\varepsilon Hf(t)$ value of 8.0, and the A/CNK and A/NK ratio of quartz diorites ranges from 1.02 to 1.04 and from 2.13 to 2.23, respectively. These features are similar to those of the type I granite, and the quartz diorite was likely derived from the lower crust. Combined with the regional geological evolution, the Gayahedonggou complex formed in a post-collision extensional environment. The pyroxene in the Gayahedonggou complex is mainly clinopyroxene, which is enriched in the CaO content, indicating that the CaO content of the parent magma of the Gayahedonggou complex is high or that the complex has been contaminated by Ca-rich surrounding rocks, which hinders Cu-Ni mineralization.

Keywords: Gayahedonggou complex; U-Pb dating; metallogenic model; East Kunlun orogenic belt; harmful crustal contamination; post-collision

1. Introduction

Magmatic Cu-Ni sulfide deposits are an important source of copper and nickel metal. Although most of the world's large magmatic Cu-Ni sulfide deposits are known to have formed in large igneous provinces [1–3], those that occur in orogenic environments also have considerable metallogenic potential [4–13]. The East Kunlun orogenic belt (EKOB), located in Northwest China (Figure 1), is considered one of the important Cu-Ni mineralization regions in all of Asia in which mafic–ultramafic intrusions are widely distributed. In the last 10 years, some magmatic Cu-Ni sulfide deposits (such as Xiarihamu, Shitoukengde, Akechukesai, and Binggounan) that formed in orogenic environments have been discovered, and the associated Ni resources reached a total of 1.2 million

tons. These Cu-Ni ore bodies occur in small ultramafic intrusions, and the formation age is between 440 and 400 Ma [4,9–11,13]; the isotope results show mantle source characteristics [5,6]. There are two views on the metallogenic model of these Cu-Ni deposits. Some researchers hold the view that the Cu-Ni deposits formed in a subducted island arc [10,12,13]. The other view is that the metallogenic environment was post-collision [4,5,14,15]. Given these different perspectives, more case studies are needed on the metallogenic model of the EKOB.
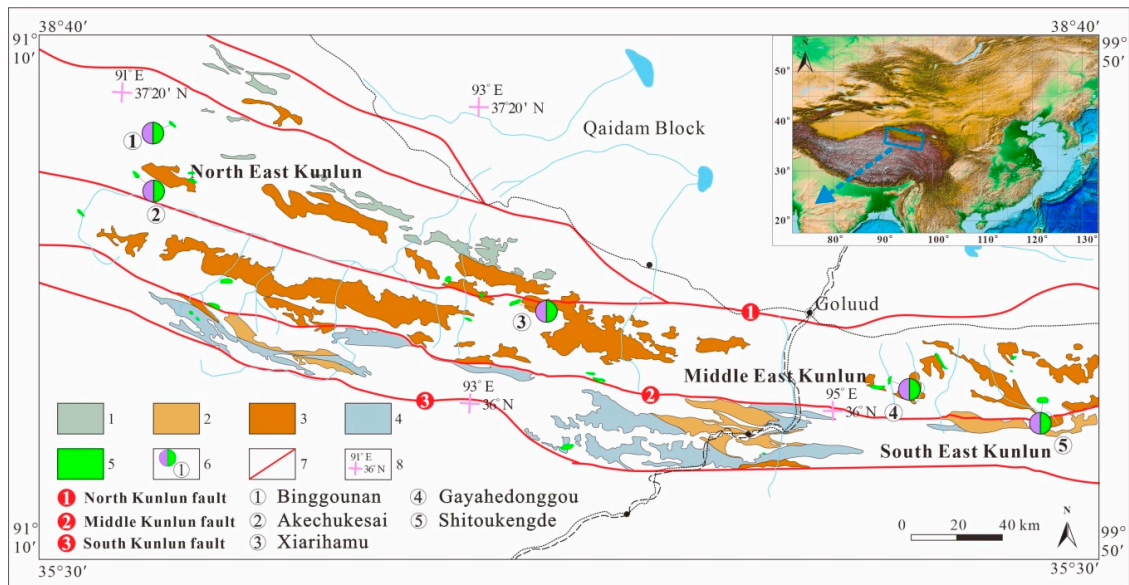

Figure 1. Geological map of the East Kunlun orogenic belt (EKOB). 1. Qimantage Group; 2. Wanbaogou Group; 3. Jinshuikou Group; 4. Nachitai Group; 5. Mafic–ultramafic intrusion; 6. Cu-Ni sulfide ore deposit; 7. Fault; 8. Longitude and latitude.

The Gayahedonggou Cu-Ni deposit was discovered by the Sichuan Nuclear Industry Geology Bureau in 2018. Preliminary geological studies suggest that the formation of the deposit is related to ultramafic intrusions at the end of the Early Paleozoic. Presently, the Ni resource reaches a total of 4 million tons, which may have the potential to be a large deposit. However, to date, no dating and isotope research has been performed on this deposit. Thus, geological samples of wehrlite (ore-bearing rock) and quartz diorite were collected from the Gayahedonggou magmatic Cu-Ni sulfide deposit. The zircon U-Pb isotopic ages of the magmatic intrusions and the petrochemical characteristics of rocks were investigated, and zircon Lu-Hf isotopic determinations were performed. The results provide new evidence for the metallogenic model of the Cu-Ni sulfide deposits in the EKOB.

2. Geology Background

2.1. Regional Geology

The EKOB belongs to the Tethys tectonic domain, which has an extremely complicated geological history [16–19]. The evolution of the Proto-Tethys began in the Precambrian and ended in the Devonian, during which the ocean basin was subducted in both directions, creating the basic tectonic framework of the EKOB [20,21]. The Paleo-Tethys evolved between the late Paleozoic and Mesozoic eras, and voluminous magmatic activity associated with the subducted oceanic crust has been recorded [22–25]. The evolution of the Neo-Tethys had little influence on the EKOB, and only a few magmatic rocks developed during this period. The north, middle, and south Kunlun faults divide the East Kunlun into the North East Kunlun orogenic belt, the Middle East Kunlun orogenic belt, and the South East Kunlun orogenic belt [26–29]; the secondary faults in the region generally develop towards the northeast (Figure 1). Regional stratigraphic outcropping is relatively complete and includes the

Paleoproterozoic Jinshuikou Group, the Mesoproterozoic Wanbaogou Group, the Cambrian-Ordovician Nachitai Group, the Qimantage Group, the Upper Devonian Maoniushan Formation, the Carboniferous Dagangou Formation, the Siyangjiao Formation, and the Upper Triassic Elashan Formation [30].

The mafic–ultramafic intrusions are mainly distributed north of the Middle Kunlun fault. The Xiarihamu deposit is the largest magmatic Cu-Ni-Co sulfide deposit in the region and the second-largest Ni deposit in China [4,5,12]. The Shitoukengde is a large-scale Cu-Ni deposit [9,16]. The ore-bearing lithologies in the belt are orthopyroxenite, websterite, harzburgite, lherzolite, and dunite, and the area is between 0.012 and 5.8 km^2 [4,5,9,13,16]. The surrounding rocks include the Jinshuikou Group and the Tanjianshan Group. Pentlandite, pyrrhotite, and chalcopyrite are the principal ore minerals in the intrusion-hosted sulfide mineralization.

2.2. Geology of the Gayahedonggou Cu-Ni Deposit

The Gayahedonggou Cu-Ni deposit is located in the Middle East Kunlun orogenic belt. The surrounding rock is the Paleoproterozoic Jinshuikou Group (Figure 2), which is the oldest metamorphic rock series in the EKOB and is composed of the Baishahe Formation and the Xiaomiao Formation [31,32]. The Baishahe Formation includes gneiss, amphibolite, and schist, and the Xiaomiao Formation is comprised of schist, gneiss, and marble. The Gayahedonggou complex consists of three mafic–ultramafic intrusions and quartz diorite. Mafic–ultramafic intrusions are comprised of wehrlite, olivine-bearing clinopyroxenite, and gabbro. The Cu-Ni ore is hosted in the wehrlite. Four Cu-Ni ore bodies have been identified. The ore bodies are 50–280 m in length and 9–34 m in thickness, with an average Ni grade of 0.415 wt%.
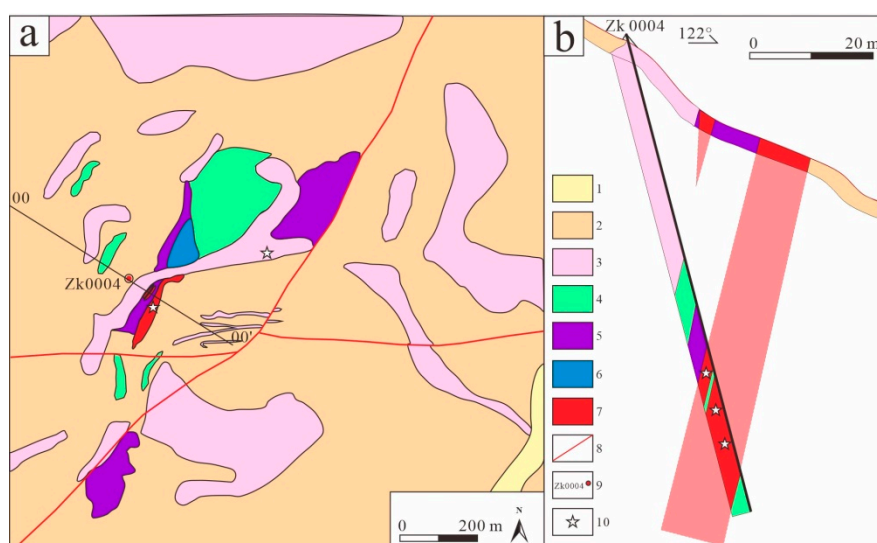

Figure 2. (**a**) Simplified geological map of the Gayahedonggou Cu-Ni deposit. (**b**) Cross sections of 00-00' in Figure 2a (modified from Sichuan Institute of Nuclear Geology, 2019). 1. Quaternary; 2. Jinshuikou Group; 3. Quartz diorite; 4. Gabbro; 5. Wehrlite; 6. Sulfide mineralization; 7. Fault; 8. Drill core; 9. Sample location.

The typical olivine-bearing clinopyroxenite contains 80% clinopyroxene and 20% olivine. The clinopyroxene and olivine crystals are 1–2 mm and 1–1.5 mm in diameter, respectively. Some pyroxenes have been altered to tremolite, and some olivine has been serpentinized (Figure 3).

Wehrlite is composed of 70% olivine, 28% clinopyroxene, and 2% sulfides. The olivine and clinopyroxene crystals are 1–2 mm and 1 mm in diameter, respectively. The sulfides are pyrrhotite (Po), pentlandite (Pn), and chalcopyrite (Cpy).

Quartz diorite contains 40% plagioclase, 25% quartz, 20% amphibole, and 15% biotite, with a crystal size of 1–2 mm.
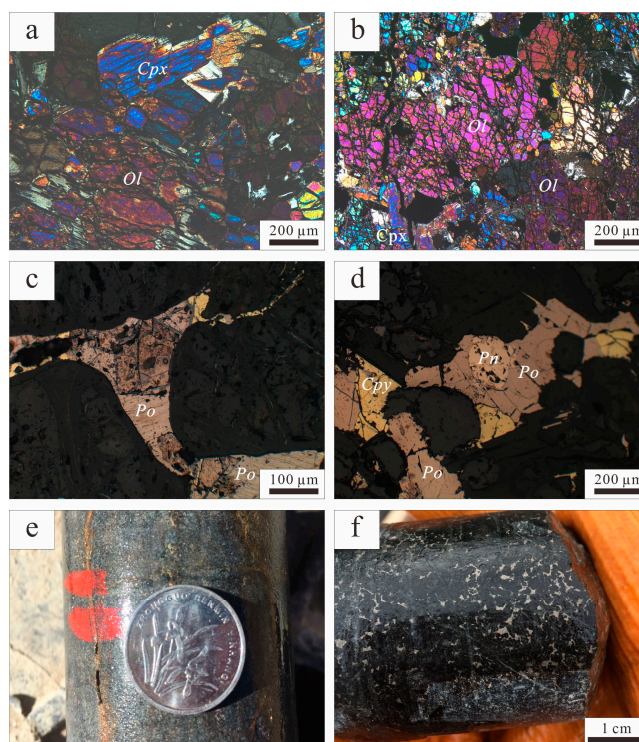
Figure 3. Hand specimens and photomicrographs of typical lithofacies from the Gayahedonggou Cu-Ni deposit. (**a**) Olivine-bearing clinopyroxenite; (**b**) Wehrlite; (**c**) Interstitial sulfide aggregates between the olivine crystals; (**d**) Wehrlite, disseminated sulfide structure; (**e**,**f**) Disseminated sulfides hosted in wehrlite from drill core ZK0004. Mineral abbreviations: Ol = olivine, Cpx = clinopyroxene, Pn = pentlandite, Po = pyrrhotite, and Cpy = chalcopyrite.

3. Sampling and Analytical Methodology

3.1. Sample Descriptions

Two samples (one wehrlite, sample location: 95°19′57.73″ E Long., 36°06′25.03″ N Lat., and one quartz diorite, sample location: 95°19′53.87″ E Long., 36°06′28.53″ N Lat.) with the least alteration were selected from the Gayahedonggou outcrops for zircon laser ablation inductively coupled plasma mass spectrometry (LA-ICP-MS) U-Pb and Lu-Hf isotopic dating. In addition, eight whole-rock samples, including wehrlite and quartz diorite, were selected for major and trace element analyses.

3.2. Zircon U-Pb and IN SITU Hf Isotope Analyses

Zircon grains were separated from bulk samples by conventional heavy-liquid and magnetic techniques and then purified by hand-picking under a binocular microscope. Representative zircon grains were mounted in epoxy resin and then polished so that the crystals were approximately sectioned in half at the Langfang Regional Geological Survey, Hebei Province, China. Zircon target and cathodoluminescence (CL) images were obtained at the State Key Laboratory of Continental Dynamics of Northwest University, Xi'an, China; zircon U-Pb determinations analysis was carried out by LA-ICP-MS at the Key Laboratory for the Study of Focused Magmatism and Giant Ore Deposits, Xi'an Center of Geological Survey, using a Geolas 2005 excimer ArF laser-ablation system coupled with an Agilent 7700 ICP-MS. Zircon isotopic determinations were obtained with a spot size of 32 μm. The detailed parameters and operating methods of the instrument have been published previously [33]. The content of common lead is low, so no correction for this parameter has been considered [34], and the zircon isotope ratio and age data were analyzed using the Glitter (ver 4.0) program for calculations and processing [35]. Isoplot 3.0 was used for age calculations and concordia plot drawings [36].

Hf isotopes were analyzed over a spot size of 44 μm, and instrumental conditions and data-acquisition procedures were similar to those described by [37]. All of the Hf analyses were carried out on the same spots that were used for U-Pb laser ablation. Zircon GJ-1 was used as the reference standard and yielded a weighted mean $^{176}Lu/^{177}Hf$ ratio of 0.282030 ± 40 (2SE) [33].

3.3. Major and Trace Element Compositions

Major and trace elements were analyzed at the Western Mineral Resources and Geological Engineering Key Laboratory of the Ministry of Education. The major elements were identified by using X-ray fluorescence spectroscopy (XRF), following the procedure of [38]. The analytical error is less than 1%. Trace elements were identified using a PQ2 Turbo ICP-MS following the technique of [39]. The precision was generally <5% for trace elements.

4. Analytical Results

4.1. Zircon U-Pb Ages

Representative CL images of zircons from the Gayahedonggou samples are shown in Figure 4. The U-Pb dating results are listed in Table 1. The zircon Th/U ratio of wehrlite is between 0.1 and 0.74, with an average of 0.33 and that of quartz diorite is between 0.27 and 0.70, with an average of 0.51. All the grains exhibit concentric zoning, indicating a magmatic zircon feature. All analyses report concordant U-Pb ages within analytical errors (Figure 4), yielding a concordia age of 419.9 ± 0.8 Ma (mean standard weighted deviation(MSWD) = 0.2) and 410.2 ± 3.5 Ma for the wehrlite and quartz diorite, respectively. These results indicate that wehrlite and quartz diorite formed during the Later Silurian and Early Devonian, respectively.
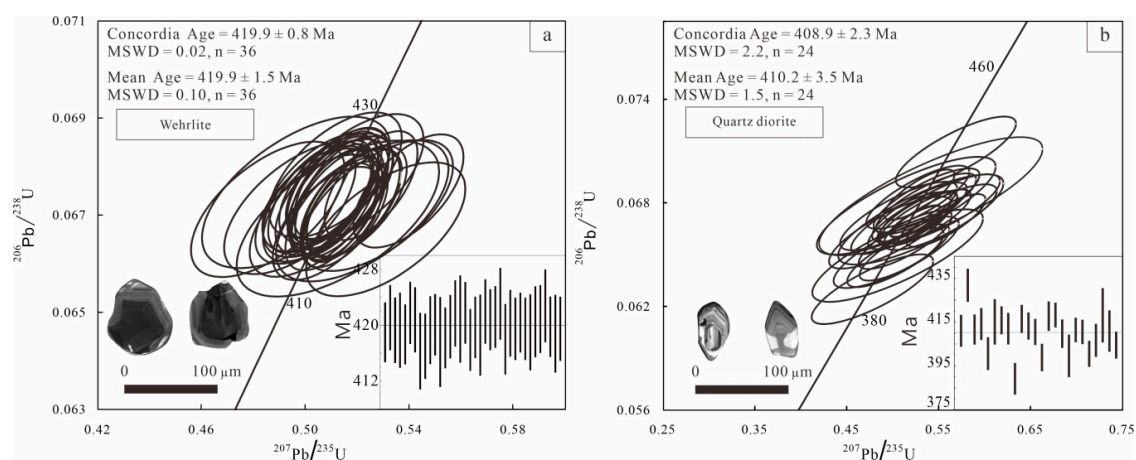

Figure 4. Concordia diagrams for zircon laser ablation inductively coupled plasma mass spectrometry (LA-ICP-MS) U-Pb dating for the Gayahedonggou Wehrlite (**a**) and Quartz diorite (**b**).

4.2. Major and Trace Elements

The major and trace element compositions of eight samples from Gayahedonggou are listed in Table 2. The LOI values range from 0.65 to 5.07 wt%, suggesting that several samples have undergone weak post-mineralization alteration. The SiO_2, MgO, TiO_2, Cr, and Ni contents in wehrlite samples are 31.52–39.70 wt%, 28.98–31.04 wt%, 0.24–0.35 wt%, 942–1394 ppm, and 1989–4438 ppm, respectively. The $Mg^{\#}$ value ranges from 0.74 to 0.79, with an average of 0.77, and the m/f $Mg^{2+}/(TFe^{2+} + Mn^{2+})$ ratio ranges from 2.84 to 3.75, with a mean value of 3.29. Quartz diorites contain 65.05–65.90 wt% SiO_2, 16.71–16.92 wt% Al_2O_3, 3.70–3.94 wt% Tfe_2O_3, and 4.96–5.15 wt% ($K_2O + Na_2O$). Quartz diorites are characterized by low K_2O content but rich CaO and Na_2O content. The A/CNK and A/NK ratios of quartz diorites range from 1.02 to 1.04 and from 2.13 to 2.23, respectively.

　　　Chondrite-normalized rare-earth element (REE) patterns and primitive mantle-normalized spidergrams for wehrlite and quartz diorite are illustrated in Figure 5. Quartz diorite and wehrlite show nearly the same pattern. They are strongly enriched in large ion lithophile element(LILEs) (Rb, Th, and K) and depleted in Nb, Ta, and Ti. The total rare-earth element contents (ΣREE) of wehrlite are low, ranging from 14.79 to 22.39 ppm. The $(La/Yb)_N$, $(La/Sm)_N$, $(Gd/Yb)_N$, Nb/U, and Ce/Pb ratios of wehrlite are 3.01–7.14, 1.69–3.91, 1.36–1.51, 2.07–2.93, and 0.55–1.42, respectively. The LREE/HREE and δEu values of quartz diorite are 5.80–6.89 and 0.97–1.06, respectively.
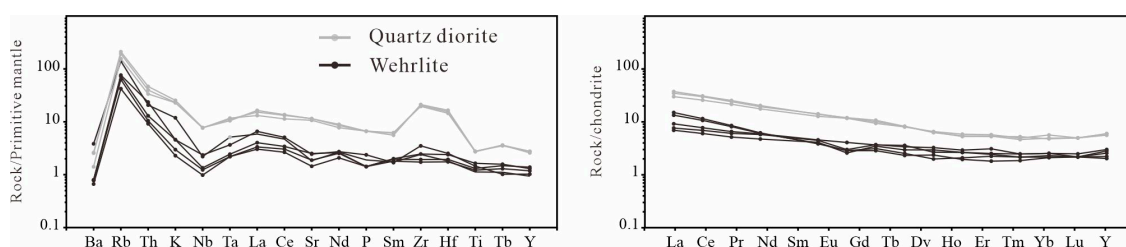

Figure 5. Primitive mantle-normalized trace element spider diagram and chondrite-normalized REE diagram (primitive mantle data after [40,41]).

4.3. Zircon Lu-Hf Isotopes

　　　The Lu-Hf isotopes of the selected zircon crystals from the wehrlite and quartz diorite are listed in Table 3. The εHf(t) values for wehrlite range from −0.8 to 4.2, with an average of 3.0. The two-stage model age (TDM2) of peridotite zircons ranges from 1.14 to 1.46 Ga, with an average of 1.24 Ga. One zircon grain from quartz diorite shows an εHf (t) value of −0.8, and the εHf(t) value of the other four grains from quartz diorite is between 5.1 and 9.9, with an average of 8.0. The two-stage model age (TDM2) of quartz diorite zircons ranges from 0.76 to 1.45 Ga, with an average of 1.01 Ga. In the εHf(t) vs. t(Ma) diagram, the data are plotted between the Hf isotopic evolution lines of chondrite and depleted mantle (Figure 6).

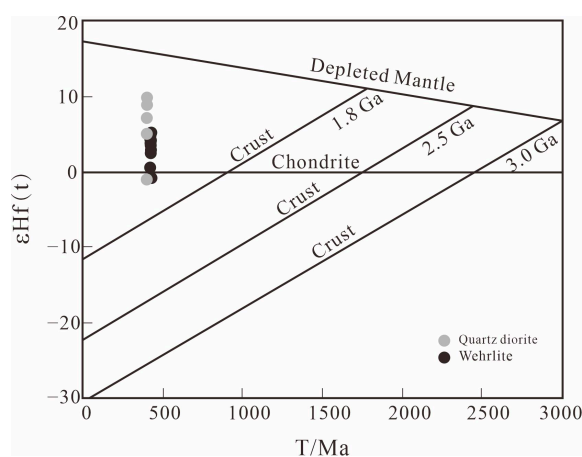**Figure 6.** Zircon εHf(t) value versus zircon U-Pb age for the Gayahedonggou wehrlite and quartz diorite.

Table 1. LA-ICP-MS zircon U-Pb dating results of wehrlite and quartz diorite.

Sample	Sample No.	(×10⁻⁶)			Th/U	Isotope Ratio						Age (Ma)					
		Pb	Th	U		$^{207}Pb/^{206}Pb$	1σ	$^{207}Pb/^{235}U$	1σ	$^{206}Pb/^{238}U$	1σ	$^{207}Pb/^{206}Pb$	1σ	$^{207}Pb/^{235}U$	1σ	$^{206}Pb/^{238}U$	1σ
	GYH01-1	83	459	1039	0.44	0.0555	0.0011	0.5140	0.0102	0.0672	0.0007	432	45	421	7	419	4
	GYH01-2	46	181	581	0.31	0.0580	0.0015	0.5395	0.0140	0.0675	0.0008	528	57	438	9	421	5
	GYH01-3	38	105	500	0.21	0.0544	0.0015	0.5044	0.0137	0.0672	0.0008	389	61	415	9	419	5
	GYH01-4	132	521	1697	0.31	0.0569	0.0021	0.5275	0.0193	0.0672	0.0009	488	81	430	13	419	5
	GYH01-5	96	343	1241	0.28	0.0557	0.0012	0.5149	0.0105	0.0671	0.0007	438	45	422	7	419	4
	GYH01-6	68	288	856	0.34	0.0563	0.0013	0.5251	0.0118	0.0676	0.0007	465	51	429	8	422	4
	GYH01-7	216	647	2813	0.23	0.0552	0.0015	0.5133	0.0135	0.0675	0.0008	420	58	421	9	421	5
	GYH01-8	42	107	566	0.19	0.0577	0.0023	0.5308	0.0202	0.0667	0.0009	518	84	432	13	416	5
	GYH01-9	54	461	620	0.74	0.0552	0.0015	0.5084	0.0139	0.0668	0.0008	419	61	417	9	417	5
	GYH01-10	56	269	697	0.39	0.0543	0.0017	0.5034	0.0150	0.0672	0.0008	384	67	414	10	419	5
	GYH01-11	76	368	952	0.39	0.0541	0.0012	0.5024	0.0111	0.0673	0.0007	376	50	413	8	420	4
	GYH01-12	46	210	598	0.35	0.0555	0.0028	0.5124	0.0257	0.0669	0.0011	433	110	420	17	418	6
	GYH01-13	127	527	1613	0.33	0.0557	0.0012	0.5148	0.0111	0.0670	0.0007	440	48	422	7	418	4
	GYH01-14	51	154	665	0.23	0.0560	0.0014	0.5196	0.0127	0.0673	0.0008	453	55	425	9	420	5
	GYH01-15	61	388	731	0.53	0.0548	0.0015	0.5110	0.0140	0.0676	0.0008	405	61	419	9	422	5
	GYH01-16	56	212	709	0.30	0.0534	0.0026	0.4963	0.0239	0.0675	0.0010	344	107	409	16	421	6
	GYH01-17	73	242	948	0.26	0.0550	0.0012	0.5123	0.0111	0.0676	0.0007	410	49	420	7	422	4
Wehrlite	GYH01-18	110	511	1381	0.37	0.0552	0.0013	0.5098	0.0116	0.0670	0.0007	420	51	418	8	418	4
	GYH01-19	92	266	1211	0.22	0.0551	0.0012	0.5108	0.0112	0.0673	0.0007	415	49	419	8	420	4
	GYH01-20	147	482	1915	0.25	0.0564	0.0024	0.5218	0.0219	0.0671	0.0010	468	93	426	15	419	6
	GYH01-21	59	296	733	0.40	0.0549	0.0014	0.5125	0.0129	0.0677	0.0008	410	56	420	9	422	5
	GYH01-22	132	534	1674	0.32	0.0548	0.0012	0.5096	0.0107	0.0675	0.0007	404	47	418	7	421	4
	GYH01-23	74	433	903	0.48	0.0549	0.0012	0.5108	0.0112	0.0675	0.0007	407	49	419	8	421	4
	GYH01-24	185	816	2324	0.35	0.0547	0.0018	0.5115	0.0168	0.0678	0.0009	400	72	419	11	423	5
	GYH01-25	197	1153	2415	0.48	0.0545	0.0018	0.5034	0.0165	0.0670	0.0008	392	72	414	11	418	5
	GYH01-26	38	194	476	0.41	0.0549	0.0016	0.5101	0.0144	0.0674	0.0008	409	62	419	10	420	5
	GYH01-27	76	357	982	0.36	0.0559	0.0013	0.5182	0.0119	0.0672	0.0007	448	51	424	8	420	4
	GYH01-28	94	542	1140	0.48	0.0550	0.0011	0.5111	0.0100	0.0674	0.0007	412	44	419	7	420	4
	GYH01-29	68	318	860	0.37	0.0553	0.0013	0.5123	0.0118	0.0673	0.0007	422	51	420	8	420	4
	GYH01-30	125	554	1591	0.35	0.0537	0.0021	0.4972	0.0189	0.0672	0.0009	358	85	410	13	419	5
	GYH01-31	148	266	1997	0.13	0.0547	0.0018	0.5085	0.0165	0.0674	0.0008	400	72	417	11	421	5
	GYH01-32	108	147	1453	0.10	0.0544	0.0016	0.5057	0.0148	0.0675	0.0008	386	65	416	10	421	5
	GYH01-33	158	480	2037	0.24	0.0555	0.0019	0.5189	0.0175	0.0678	0.0009	433	75	424	12	423	5
	GYH01-34	171	718	2152	0.33	0.0550	0.0011	0.5103	0.0104	0.0673	0.0007	413	45	419	7	420	4
	GYH01-35	160	575	2080	0.28	0.0525	0.0022	0.4854	0.0195	0.0671	0.0009	305	91	402	13	419	6
	GYH01-36	99	374	1269	0.29	0.0558	0.0014	0.5175	0.0129	0.0672	0.0008	445	55	424	9	420	5

Table 1. *Cont.*

Sample	Sample No.	(×10⁻⁶)			Th/U	Isotope Ratio							Age (Ma)					
		Pb	Th	U		$^{207}Pb/^{206}Pb$	1σ	$^{207}Pb/^{235}U$	1σ	$^{206}Pb/^{238}U$	1σ	$^{207}Pb/^{206}Pb$	1σ	$^{207}Pb/^{235}U$	1σ	$^{206}Pb/^{238}U$	1σ
	GYH02-1	22	154	260	0.59	0.0563	0.0027	0.5110	0.0238	0.0659	0.0010	462	103	419	16	411	6
	GYH02-2	17	113	231	0.49	0.0560	0.0033	0.5353	0.0311	0.0693	0.0012	453	127	435	21	432	7
	GYH02-3	20	117	237	0.50	0.0576	0.0033	0.5231	0.0292	0.0659	0.0011	513	121	427	19	411	7
	GYH02-4	20	166	236	0.70	0.0571	0.0035	0.5224	0.0313	0.0663	0.0012	495	130	427	21	414	7
	GYH02-5	16	87	197	0.44	0.0553	0.0037	0.4886	0.0324	0.0641	0.0012	424	144	404	22	400	7
	GYH02-6	22	155	260	0.59	0.0542	0.0051	0.4965	0.0462	0.0665	0.0017	377	200	409	31	415	10
	GYH02-7	15	76	188	0.40	0.0558	0.0029	0.5120	0.0259	0.0666	0.0010	442	111	420	17	416	6
	GYH02-8	19	112	233	0.48	0.0539	0.0034	0.4905	0.0303	0.0660	0.0012	368	135	405	21	412	7
	GYH02-9	16	95	195	0.49	0.0548	0.0037	0.4700	0.0314	0.0622	0.0012	405	146	391	22	389	7
	GYH02-10	21	138	258	0.53	0.0557	0.0030	0.5124	0.0274	0.0668	0.0011	438	117	420	18	417	7
	GYH02-11	16	92	203	0.45	0.0556	0.0027	0.5068	0.0245	0.0662	0.0010	434	106	416	17	413	6
Quartz diorite	GYH02-12	19	120	239	0.50	0.0554	0.0026	0.5016	0.0232	0.0657	0.0010	427	102	413	16	410	6
	GYH02-13	22	168	263	0.64	0.0555	0.0029	0.4881	0.0250	0.0638	0.0010	431	113	404	17	399	6
	GYH02-14	17	102	219	0.47	0.0548	0.0029	0.5055	0.0267	0.0669	0.0011	403	116	415	18	418	7
	GYH02-15	19	108	236	0.46	0.0548	0.0020	0.5066	0.0182	0.0671	0.0009	404	80	416	12	418	5
	GYH02-16	23	84	311	0.27	0.0545	0.0029	0.4926	0.0259	0.0656	0.0011	390	116	407	18	410	6
	GYH02-17	17	98	211	0.46	0.0556	0.0051	0.4897	0.0441	0.0639	0.0016	435	193	405	30	399	10
	GYH02-18	15	78	188	0.42	0.0556	0.0023	0.5049	0.0207	0.0659	0.0009	436	90	415	14	411	6
	GYH02-19	27	199	322	0.62	0.0582	0.0023	0.5274	0.0205	0.0657	0.0009	537	85	430	14	410	5
	GYH02-20	19	129	236	0.55	0.0561	0.0027	0.4951	0.0232	0.0641	0.0010	454	103	408	16	400	6
	GYH02-21	21	142	257	0.55	0.0539	0.0036	0.4841	0.0318	0.0651	0.0012	368	144	401	22	407	7
	GYH02-22	18	108	231	0.47	0.0559	0.0064	0.5157	0.0578	0.0670	0.0020	446	236	422	39	418	12
	GYH02-23	14	93	180	0.52	0.0560	0.0048	0.5078	0.0427	0.0658	0.0015	452	180	417	29	411	9
	GYH02-24	20	139	249	0.56	0.0556	0.0028	0.4957	0.0241	0.0647	0.0010	434	106	409	16	404	6

Table 2. Major elements (%) and trace elements (10^{-6}) of wehrlite and quartz diorite.

Rock Type	Wehrlite					Quartz Diorite		
Sample No.	a1	a2	a3	a4	a5	a6	a7	a8
Sample Location	ZK0004 72–85 m					E 95°19′53.87″, N 36°06′28.53″		
SiO_2	39.70	31.67	34.36	37.16	31.52	65.68	65.05	65.90
TiO_2	0.28	0.35	0.31	0.26	0.24	0.58	0.59	0.59
Al_2O_3	2.63	14.31	9.14	2.57	12.16	16.76	16.71	16.92
MnO	0.14	0.09	0.08	0.10	0.06	0.06	0.07	0.07
MgO	30.09	28.98	31.04	30.47	29.59	1.55	1.79	1.60
CaO	3.22	3.12	2.69	2.85	1.97	4.71	4.73	4.81
Na_2O	0.35	0.47	0.32	0.20	0.37	3.96	4.04	3.96
K_2O	0.13	0.20	0.20	0.10	0.52	1.01	1.11	1.00
P_2O5	0.03	0.03	0.05	0.03	0.04	0.14	0.14	0.14
Tfe_2O_3	19.20	16.34	16.36	21.23	17.86	3.70	3.94	3.81
LOI	3.79	3.78	5.07	4.50	5.00	0.72	0.93	0.65
Total	99.56	99.34	99.62	99.47	99.33	98.87	99.10	99.45
La	2.37	2.85	4.66	2.15	4.15	10.78	11.61	9.31
Ce	5.58	6.26	9.31	4.87	8.62	24.23	24.95	20.81
Pr	0.74	0.80	1.04	0.63	0.99	2.94	3.09	2.63
Nd	3.46	3.56	3.72	2.84	3.64	11.62	12.21	10.57
Sm	0.87	0.89	0.75	0.80	0.77	2.76	2.71	2.48
Eu	0.22	0.30	0.21	0.19	0.21	0.87	0.88	0.86
Gd	0.96	0.95	0.74	0.90	0.81	2.61	2.78	2.43
Tb	0.16	0.17	0.11	0.14	0.12	0.39	0.39	0.38
Dy	1.05	0.86	0.76	0.95	0.64	2.02	2.06	2.11
Ho	0.21	0.19	0.14	0.19	0.15	0.39	0.38	0.42
Er	0.65	0.53	0.38	0.51	0.47	1.13	1.11	1.20
Tm	0.08	0.08	0.06	0.07	0.07	0.15	0.17	0.16
Yb	0.53	0.53	0.44	0.48	0.45	1.03	1.00	1.18
Lu	0.08	0.07	0.07	0.07	0.07	0.16	0.16	0.16
Y	6.30	5.92	4.66	5.38	4.26	12.57	11.78	12.53
Rb	5.45	5.48	5.59	4.65	26.81	17.84	18.27	9.85
Ba	39.91	45.97	48.39	26.79	89.07	122.62	134.16	98.98
Th	0.88	1.09	1.98	0.77	1.74	3.35	3.91	2.82
U	0.30	0.39	0.64	0.28	0.76	0.52	0.51	0.47
Ta	0.09	0.10	0.15	0.09	0.21	0.46	0.43	0.48
Nb	0.88	0.96	1.68	0.70	1.57	5.52	5.52	5.45
Sr	39.70	53.09	51.69	30.45	38.80	242.32	241.11	225.10
Zr	21.63	27.52	39.26	19.37	26.96	219.41	228.90	237.11
Hf	0.60	0.74	0.78	0.54	0.56	4.48	4.79	5.10
Pb	4.03	11.34	7.82	3.60	6.06	5.89	6.04	5.68
Ga	3.74	16.58	9.63	3.74	13.31	18.69	18.25	17.90
Zn	64.21	214.52	102.52	68.44	152.40	44.04	43.22	40.82
$K_2O + Na_2O$	0.48	0.67	0.52	0.30	0.89	4.97	5.15	4.96
K_2O/Na_2O	0.37	0.43	0.63	0.50	1.41	0.26	0.27	0.25
A/CNK	0.40	2.15	1.62	0.46	2.56	1.04	1.02	1.04
A/NK	3.67	14.46	12.30	5.88	10.38	2.20	2.13	2.23
ΣREE	16.96	18.04	22.39	14.79	21.16	61.08	63.50	54.70
ΣLREE	13.24	14.66	19.69	11.48	18.38	53.20	55.45	46.66
ΣHREE	3.72	3.38	2.70	3.31	2.78	7.88	8.05	8.04
LREE/HREE	3.56	4.34	7.29	3.47	6.61	6.75	6.89	5.80
$(La/Yb)_N$	3.01	3.63	7.14	3.02	6.22	7.06	7.83	5.32
$(La/Sm)_N$	1.71	2.01	3.91	1.69	3.39	2.46	2.69	2.36
$(Gd/Yb)_N$	1.46	1.45	1.36	1.51	1.45	2.04	2.24	1.66
δEu	0.73	0.99	0.85	0.68	0.81	0.98	0.97	1.06
δCe	1.01	0.98	0.98	1.00	0.99	1.02	0.98	1.00
m/f	3.08	3.50	3.75	2.84	3.28	-	-	-
Nb/U	2.93	2.46	2.63	2.50	2.07	-	-	-
Ce/Pb	1.38	0.55	1.19	1.35	1.42	-	-	-

Note: LOI = Loss on ignition; A/CNK = $Al_2O_3/(CaO + Na_2O + K_2O)$; A/NK = $Al_2O_3/(Na_2O + K_2O)$; m/f = $Mg^{2+}/(TFe^{2+} + Mn^{2+})$; LREE = light rare-earth element; HREE = heavy rare-earth element.

Table 3. Zircon Hf isotopic compositions of wehrlite and quartz diorite.

Sample	Analysis Spot	t(Ma)	^{176}Yb/^{177}Hf	^{176}Lu/^{177}Hf	^{176}Hf/^{177}Hf	2σ	(^{176}Hf/^{177}Hf)i	εHf(t)	2σ	T$_{DM1}$(Ma)	T$_{DM2}$(Ma)
	GYH01-5	419	0.004561	0.000148	0.282623	0.000029	0.28262	3.9	1.0	872	1157
	GYH01-6	422	0.009725	0.000338	0.282489	0.000061	0.28249	−0.8	2.2	1062	1458
	GYH01-8	416	0.008986	0.000295	0.282521	0.000034	0.28252	0.2	1.2	1016	1389
	GYH01-9	417	0.029368	0.000731	0.282620	0.000044	0.28261	3.6	1.6	890	1174
Wehrlite	GYH01-13	418	0.008110	0.000253	0.282616	0.000029	0.28261	3.6	1.0	883	1173
	GYH01-18	418	0.014775	0.000443	0.282600	0.000026	0.28260	3.0	0.9	910	1213
	GYH01-19	420	0.010267	0.000362	0.282600	0.000036	0.28260	3.0	1.3	909	1212
	GYH01-27	420	0.008042	0.000318	0.282583	0.000047	0.28258	2.4	1.6	931	1248
	GYH01-33	423	0.009852	0.000321	0.282629	0.000034	0.28263	4.2	1.2	867	1143
	GYH01-34	420	0.012324	0.000398	0.282594	0.000033	0.28259	2.8	1.1	918	1225
	GYH02-2	432	0.04142	0.001094	0.282784	3.7584×10^{-5}	0.282776	9.6	1.3	666	803
	GYH02-12	410	0.039993	0.00105	0.28267	3.80829×10^{-5}	0.282662	5.1	1.3	826	1071
Quartz diorite	GYH02-16	410	0.043683	0.001153	0.282731	4.29311×10^{-5}	0.282722	7.2	1.5	742	937
	GYH02-18	411	0.0483	0.001238	0.282808	3.84727×10^{-5}	0.282798	9.9	1.3	634	764
	GYH02-23	411	0.031246	0.000792	0.282501	3.28299×10^{-5}	0.282495	−0.8	1.1	1058	1446

$\lambda = 1.867 \times 10^{-11}$/a; (^{176}Lu/^{177}Hf) $_{CHUR}$ = 0.0332 [42]; (^{176}Hf/^{177}Hf)CHUR, 0 = 0.282772 [43]; (^{176}Lu/^{177}Hf)$_{DM}$ = 0.0384, (^{176}Hf/^{177}Hf)$_{DM}$ = 0.28325 [44]; fs = f$_{Lu/Hf}$; f$_{DM}$ = [(^{176}Lu/^{177}Hf)DM/(^{176}Lu/^{177}Hf) CHUR] − 1.

5. Discussion

5.1. Source

5.1.1. Wehrlite Source and Crustal Contamination

The average εHf(t) value of the wehrlite from the Gayahedonggou complex is 3.0. Such high εHf(t) values indicate that the Gayahedonggou wehrlite is unlikely to have been derived from the continental lithospheric mantle, which is characterized by εHf(t) values of less than 0 [44]. Consequently, this study concludes that the Gayahedonggou wehrlite was likely derived from a depleted mantle or the asthenosphere. The ratios of elements with similar atomic numbers are not easily affected by the evolution of magmatic rocks; therefore, Th/Yb, Zr/Yb, Nb/U, Ce/Yb, etc., are useful proxies for evaluating the role of upper/lower crustal contamination vs. mantle source enrichment [45–47]. In Figure 7a,b, Zr is positively correlated with Th, and the ratios of Th/Yb and Nb/La show a weak positive correlation. Mid-Oceanic Ridge Basalts(MORB) and Oceanic-Island Basalt(OIB)have high, uniform Nb/U ratios of 47 ± 10 [48]. In contrast, the Nb/U ratio of the Gayahedonggou wehrlite is 2.51–2.06, which is similar to the mean values of the continental crust (~9.7) [49]. The average Ce/Pb ratio of the mantle is 25 ± 5, whereas that of the continental crust is <15 [50]. The Ce/Pb ratios of the Gayahedonggou intrusion range from 0.55 to 1.42, which differ from mantle values but are relatively similar to those of the continental crust, suggesting significant crustal contamination.
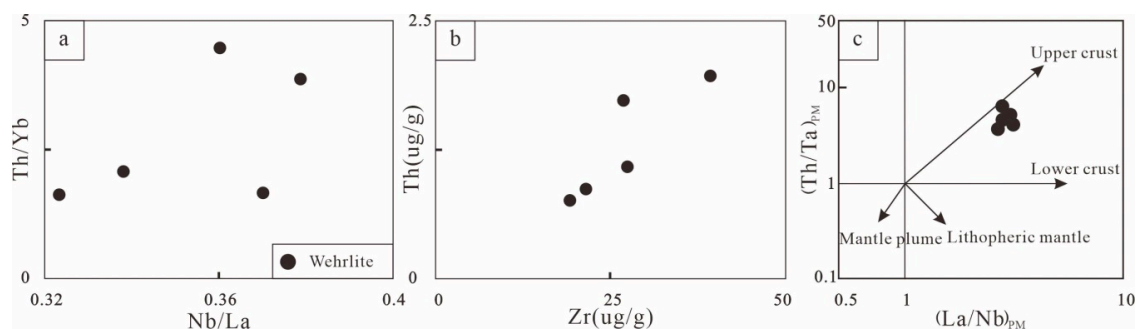
Figure 7. Plots of selected trace elements for evaluating contamination processes of the Gayahedonggou wehrlite. Figure 7c is modified from [51]. (**a**) Nb/La-Th/Yb; (**b**) Zr/Th; (**c**) (La/Nb)$_{PM}$-(Th/Ta)$_{PM}$ diagrams for the Gayahedonggou wehrlite.

The values of (La/Nb)$_{PM}$ and (Th/Ta)$_{PM}$ of the upper and lower crusts are markedly different and can be used to identify crustal contamination materials [51]. In Figure 7c, which considers these parameters, the wehrlite data plot towards the upper crust field. In summary, the Gayahedonggou wehrlite originated from a depleted mantle, and the material was added to the original magma through upper-crustal contamination.

5.1.2. The Source of Quartz Diorite

Generally, there are four types of granite: S-, I-, A-, and M-type granite. A-type granite is generally anhydrous and is characterized by low CaO, Sr, Ti, P, and Ba contents and high $Na_2O + K_2O$, Rb, Zr, Ga, and SiO_2 contents and Ga/Al ratios [52,53]. I-type granites commonly contain amphibole, apatite, and titanite, with (A/CNK) ratios < 1.1 and $Na_2O > K_2O$. Typical S-type granites often contain minerals such as muscovite, cordierite, and garnet, with A/CNK ratios > 1.1 [54]. The MgO and Na_2O contents of quartz diorite are relatively high, and the A/CNK and A/NK ratios range from 1.02 to 1.04 and from 2.13 to 2.23, respectively. In the A/CNK-A/NK figure, the data for the quartz diorite samples are plotted within the I-type granite area (Figure 8a). Quartz diorite is composed of plagioclase, amphibole, quartz, and biotite. In Figure 8b, the quartz diorite samples fall in the peraluminous region and the tholeiite to calc-alkaline series region. The aforementioned features correspond to the

I-type granite in the EKOB during the same period. Furthermore, a geological field investigation reveals that mafic microgranular enclaves (MMEs), which are considered to have originated from the mixing of lower-crust- and enriched mantle-derived magmas, exist in the quartz diorite samples [55,56]. The Rb/Sr values of quartz diorite are between 0.04 and 0.07, which are significantly lower than the crustal ratio (5.36~6.55) [40]. Moreover, the average εHf(t) of quartz diorite is 8.0; such high εHf(t) values generally reflect the typical characteristics of the mantle. This does not display the features expected of A-type granite based on the major elements; thus, it is unlikely that the quartz diorite was derived from the mantle. Therefore, the quartz diorite was likely derived from the lower crust, which is a mixture of the mantle and the crust magma region.
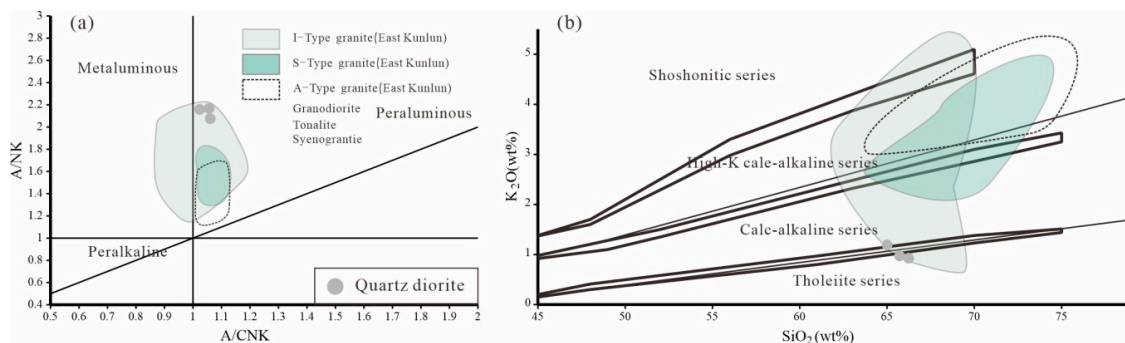
Figure 8. A/CNK-A/NK (**a**) and SiO_2-K_2O (**b**) diagrams for the Gayahedonggou quartz diorite. The fields are similar magmatic rocks in the EKOB (these data come from geological maps (1:50,000, 1:250,000)). Figure 8a is modified from [57]; Figure 8b is modified from [58,59].

5.2. Tectonic Setting

It has been confirmed that the EKOB entered the stage of Proto-Tethys evolution in the Cambrian [60–62]. Magmatic rocks with ages of 515–436 Ma generally have island arc characteristics, and the lithologies include diorite, andesite, and gabbro. After 428 Ma, A-type and peraluminous granites appeared in large quantities, and the nature of magmatic rocks changed from island arc to intracontinental [63,64]. Moreover, eclogite, which is formed under ultra-high pressure, also provides evidence to support these findings. The formation age of eclogite in the Xiarihamu is 437 ± 3.6 Ma [65], while that in the Wenquan is 451 ± 2 Ma [66]. This indicates that there was a deep subduction event in the EKOB at the end of the early Paleozoic; the collision was completed at approximately 428 Ma (Figure 9a), and the region entered the post-collision extension stage [5,60].

There are two views on the metallogenic model for the late Paleozoic magmatic Cu-Ni sulfide deposits in the EKOB. One theory is the subduction island arc environment metallogenic model [10,12,13], which posits that the genesis of ore-bearing intrusions was controlled by the Proto-Tethys subduction process. The deep subduction of oceanic crust resulted in the partial melting of the lithospheric mantle and Cu-Ni enrichment and mineralization [13]. However, the $Fe^{3+}/\sum Fe$ ratio of Cr-spinel for the Alaskan-type ultramafic intrusions, which is in the arc setting, is >0.3; in contrast, this ratio for the ultramafic in the post-collision, or rift, setting is <0.3 [5]. The $Fe^{3+}/\sum Fe$ ratio of Cr-spinel from the Xiarihamu giant Ni-Co deposit in the EKOB is <0.3 [5], indicating that it was not in the arc environment. The other theory is the post-collision extensional environment metallogenic model [4,5,14,15], which is supported by reginal tectonic evolution. The age of the wehrlite of the Gayahedonggou complex is 419.9 ± 0.8 Ma. A high εHf(t) value indicates that the Gayahedonggou complex was likely derived from a depleted mantle or the asthenospheric mantle. In the Th/Yb- Nb/Yb diagram (Figure 10a), wehrlite samples are located at the MORB–OIB evolution line and tend to approach the volcanic arc region, reflecting the influence of subduction components [67]. At the same time, the Th/Nb and Th/Yb ratios are relatively small, which suggests the presence of a large amount of subduction-related fluid in the source region. In the Nb/Zr vs. Th/Zr diagram, the trends of the samples are consistent with that of

subduction-fluid metasomatism (Figure 10b). The addition of this subduction-related fluid resulted in the geochemical characteristics of island arc magmatic rocks in the source region, but this does not mean that these intrusions formed in the arc environment [18]. At the end of the late Paleozoic, the Proto-Tethys Ocean completed subduction at approximately 428 Ma, it entered the post-collision extension stage, and slab break-off occurred [5,60].
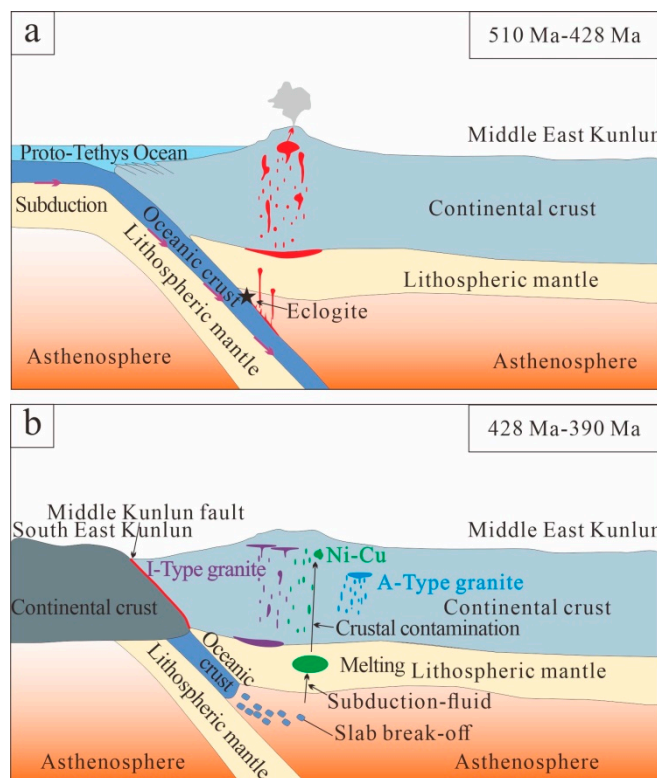

Figure 9. Geological evolution in the EKOB between 510 and 390 Ma. (**a**) The Proto - Tethys Ocean subducted between 510 and 428 Ma.; (**b**) The post-collision extension setting between 428 and 390 Ma.
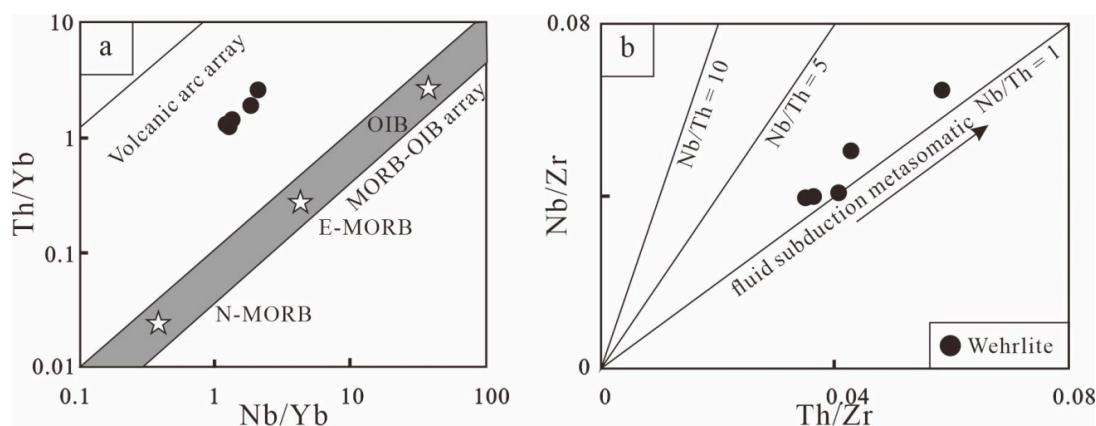
Figure 10. Nb/Yb-Th/Yb (**a**) and Th/Zr-Nb/Zr (**b**) diagrams. Figure 10a is modified from [47] and Figure 10b is modified from [68].

Some A-type granites with low CaO, MgO, and Sr contents in the EKOB are considered to have formed in the post-collision environment, such as the Nniantang A-type syenogranite (403 ± 2 Ma) [69]. To date, the latest Paleozoic A-type granite reported in the East Kunlun area is the Binggou granite with an age of 391 ± 3 Ma [70]. Thus, the post-collision extension setting appears to have lasted up to approximately 390 Ma. These mafic–ultramafic rocks and those of the Gayahedonggou complex

formed at 420 Ma and 410 Ma, respectively. Thus, it is reasonable to posit that the mafic–ultramafic rocks and quartz diorite in the Gayahedonggou complex formed in the post-collision extension setting (Figure 9b).

5.3. Cu-Ni Mineralization Potential

The Cu-Ni deposit in the EKOB formed between the late Early Paleozoic and the early Late Paleozoic. Some Cu-Ni deposits have been discovered in the eastern and western parts of the EKOB. However, no Cu-Ni deposits exist in the central area of the EKOB before the discovery of the Gayahedonggou deposit. Thus, the discovery of the Gayahedonggou deposit indicates that a Cu-Ni metallogenic belt spans 800 km in the EKOB.

Liu et al. (2019a) summarized that the large Cu-Ni deposit in the EKOB shares the following characteristics: (1) the mafic–ultramafic complexes have a broader range of m/f values ($m/f_{max} - m/f_{min} > 2.5$) and higher m/f values ($m/f_{max} > 5.5$); (2) the pyroxene in the intrusion is mainly orthopyroxene; and (3) the olivine and the clinopyroxene in mineralized intrusions contain low contents of FeO and CaO [17]. The highest m/f ratio is 3.75 in the Gayahedonggou complex, which is much lower than 5.5. Typically, only the m/f ratio of dunite in the EKOB could reach 5.5. This is consistent with the lack of dunite found in the Gayahedonggou deposit. This reflects the fact that the ultramafic magma in the Gayahedonggou complex is not much stronger than that in the large Cu-Ni deposits in the EKOB. The pyroxene in the Gayahedonggou complex is mainly clinopyroxene, which is enriched in the CaO content, indicating that the CaO content of the parent magma of the Gayahedonggou complex is high or that the complex has been contaminated by Ca-rich surrounding rocks. During the crustal contamination process, the crustal components that promote sulfide saturation were defined as "beneficial crustal contamination"; in contrast, the crustal components that hinder sulfide saturation were defined as "harmful crustal contamination" [71]. The introduction of calcite marble is regarded as typical "harmful crustal contamination", because it increases the CaO content of the magma, which hinders sulfide saturation [9,72]. High-temperature and high-pressure experiments also show that the contamination of $CaCO_3$ inhibits sulfide saturation of the mafic–ultramafic magma [73]. Meanwhile, the Gayahedonggou complex is characterized by a high CaO feature, which hinders Cu-Ni mineralization.

6. Conclusions

Important conclusions from this study are as follows:

1. The zircon U-Pb ages of ore-bearing wehrlite and quartz diorite are 419.9 ± 1.5 and 410.2 ± 3.5 Ma, respectively. According to Lu-Hf isotope and geochemical analyses, wehrlite was likely derived from a depleted mantle or the asthenosphere, and the source region of quartz diorite is likely the lower crust.
2. The parental magma of the wehrlite was modified by subduction-related fluids.
3. The Gayahedonggou complex formed in a post-collision extensional environment.
4. The pyroxene in the Gayahedonggou complex is mainly clinopyroxene, which is enriched in the CaO content, indicating that the CaO content of the parent magma of the Gayahedonggou complex is high or that the complex has been contaminated by Ca-rich surrounding rocks, which hinders Cu-Ni mineralization.

Conflicts of Interest: The authors declare no conflict of interest.

References

1. Xu, Y.G.; Chung, S.L.; Jahn, B.M.; Wu, G.Y. Petrologic and geochemical constraints on the petrogenesis of Permian-Triassic Emeishan flood basalts in southwestern China. *Lithos* **2001**, *58*, 145–168. [CrossRef]

2. Tao, Y.; Putirka, K.; Hu, R.Z.; Li, C.S. The magma plumbing system of the Emeishan large igneous province and its role in basaltic magma differentiation in a continental setting. *Am. Mineral.* **2015**, *100*, 2509–2517. [CrossRef]

3. Liu, Y.G.; Lü, X.B.; Wu, C.M.; Duan, L.; Deng, G.; Wang, H.; Zhu, X.K.; Zeng, H.D.; Wang, P.; Wang, W.; et al. The migration of Tarim plume magma toward the northeast in Early Permian and its significance for the exploration of PGE-Cu-Ni magmatic sulfide deposits in Xinjiang, NW China: As suggested by Sr-Nd-Hf isotopes, sedimentology and geophysical data. *Ore Geol. Rev.* **2016**, *72*, 538. [CrossRef]

4. Song, X.Y.; Yi, J.N.; Chen, L.M.; Yu, S.Y.; Liu, C.Z.; Dang, X.Y.; Yang, Q.A.; Wu, S.K. The Giant Xiarihamu Ni-Co Sulfide Deposit in the East Kunlun Orogenic Belt, Northern Tibet Plateau, China. *Econ. Geol.* **2016**, *111*, 29–55. [CrossRef]

5. Liu, Y.G.; Li, W.Y.; Jia, Q.Z.; Zhang, Z.W.; Wang, Z.A.; Zhang, Z.B.; Zhang, J.W.; Qian, B. The dynamic sulfide saturation process and a possible slab break-off model for the Giant Xiarihamu magmatic nickel ore deposit in the East Kunlun Orogenic Belt, Northern Qinghai-Tibet Plateau, China. *Econ. Geol.* **2018**, *113*, 1383–1417. [CrossRef]

6. Wang, X.; Zhang, M.; Fu, Y.; Zhang, J.; Li, L.; Tang, Q.; Li, Z. The magmatic intrusive direction constrains from noble gas isotopic compositions: A case study of the Xiarihamu Ni-Cu sulfide deposit in East Kunlun orogenic belt. *Acta Petrol. Sin.* **2018**, *34*, 3433–3444. (In Chinese)

7. Feng, Y.Q.; Qian, Z.Z.; Duan, J.; Xu, G.; Ren, M.; Jiang, C. Geochronological and geochemical study of the Baixintan magmatic Ni-Cu sulphide deposit: New implications for the exploration potential in the western part of the East Tianshan nickel belt (NW China). *Ore Geol. Rev.* **2018**, *95*, 366–381. [CrossRef]

8. Zhang, J.Y.; Lei, H.L.; Ma, C.Q.; Li, J.W.; Pan, Y.M. Geochemical and thermodynamical modeling of magmatic sources and processes for the Xiarihamu sulfide deposit in the eastern Kunlun Orogen, western China. *J. Geochem. Explor.* **2018**, *190*, 345–356. [CrossRef]

9. Zhang, Z.W.; Wang, Y.L.; Qian, B.; Liu, Y.G.; Zhang, D.Y.; Lü, P.R.; Dong, J. Metallogeny and tectonomagmatic setting of Ni-Cu magmatic sulfide mineralization, number I Shitoukengde mafic-ultramafic complex, East Kunlun Orogenic Belt, NW China. *Ore Geol. Rev.* **2018**, *96*, 236–246. [CrossRef]

10. Jiang, C.Y.; Ling, J.L.; Zhou, W.; Du, W.; Wang, Z.X.; Fan, Y.Z.; Song, Y.F.; Song, Z.B. Petrogenesis of the Xiarihamu Ni-bearing layered mafic-ultramafic intrusion, East Kunlun: Implications for its extensional island arc environment. *Acta Petrol. Sin.* **2015**, *31*, 1117–1136. (In Chinese)

11. Qian, Y.; Li, H.R.; Sun, F.Y.; Sun, J.; Wang, G. Zircon U-Pb dating and sulfide Re-Os isotopes of the Xiarihamu Cu-Ni sulfide deposit in Qinghai Province, Northwestern China. *Can. J. Earth Sci.* **2020**, *57*, 885–902.

12. Du, W. Study on the Mafic-Ultramafic Rocks of Xiarihamu Nickel Mining Area in East Kunlun. Ph.D. Thesis, Chang'an University, Xi'an, China, 2015. (In Chinese).

13. Li, C.S.; Zhang, Z.W.; Li, W.Y.; Wang, Y.L.; Sun, T.; Ripley, E.M. Geochronology, petrology and Hf–S isotope geochemistry of the newly-discovered Xiarihamu magmatic Ni–Cu sulfide deposit in the Qinghai–Tibet plateau, western China. *Lithos* **2015**, *216–217*, 224–240. [CrossRef]

14. Peng, B.; Sun, F.Y.; Li, B.L.; Wang, G.; Li, S.J.; Zhao, T.F.; Li, L.; Zhi, Y.B. The geochemistry and geochronology of the Xiarihamu II mafic–ultramafic complex, Eastern Kunlun, Qinghai Province, China: Implications for the genesis of magmatic Ni–Cu sulfide deposits. *Ore Geol. Rev.* **2016**, *73*, 13–28. [CrossRef]

15. Zhang, Z.W.; Wang, Y.L.; Wang, C.Y.; Qian, B.; Li, W.Y.; Zhang, J.W.; You, M.X. Mafic-ultramafic magma activity and copper-nickel sulfide metallogeny during Paleozoic in the Eastern Kunlun Orogenic Belt, Qinghai Province, China. *China Geol.* **2019**, *2*, 467–477. (In Chinese) [CrossRef]

16. Li, L.; Sun, F.Y.; Li, B.L.; Li, S.J.; Chen, G.J.; Wang, W.; Yan, J.M.; Zhao, T.F.; Dong, J.; Zhang, D.X. Geochronology, Geochemistry and Sr-Nd-Pb-Hf Isotopes of No. I Complex from the Shitoukengde Ni–Cu sulfide deposit in the Eastern Kunlun Orogen, Western China: Implications for the MAGMATIC source, geodynamic setting and genesis. *Acta Geol. Sin. Engl. Ed.* **2018**, *92*, 106–126. [CrossRef]

17. Liu, Y.G.; Chen, Z.G.; Li, W.Y.; Xu, X.H.; Kou, X.; Jia, Q.Z.; Zhang, Z.W.; Liu, F.; Wang, Y.L.; You, M.X. The Cu-Ni mineralization potential of the Kaimuqi mafic-ultramafic complex and the indicators for the magmatic Cu-Ni sulfide deposit exploration in the East Kunlun Orogenic Belt, Northern Qinghai-Tibet Plateau, China. *J. Geochem. Explor.* **2019**, *198*, 41–53. [CrossRef]

18. Li, W.Y.; Wang, Y.L.; Qian, B.; Liu, Y.G.; Han, Y.X. Discussion on formation of magmatic Cu-Ni-Co sulfide deposits in margin of Tarim Block. *Earth Sci. Front.* **2020**, *27*, 276–293. (In Chinese) [CrossRef]

19. Zhao, X.; Wei, J.H.; Fu, L.B.; Huizenga, J.M.; Santosh, M.; Chen, J.J.; Wang, D.Z.; Li, A.B. Multi-stage crustal melting from Late Permian back-arc extension through Middle Triassic continental collision to Late Triassic post-collisional extension in the East Kunlun Orogen. *Lithos* **2020**, *360–361*, 105446. [CrossRef]

20. Zhang, J.Y.; Ma, C.Q.; Xiong, F.H.; Liu, B.; Li, J.W.; Pan, Y.M. Early Paleozoic high-Mg diorite-granodiorite in the eastern Kunlun Orogen, western China: Response to continental collision and slab break-off. *Lithos* **2014**, *210–211*, 129–146. [CrossRef]

21. Dong, Y.P.; He, D.F.; Sun, S.S.; Liu, X.M.; Zhou, X.H.; Zhang, F.F.; Yang, Z.; Cheng, B.; Zhao, G.C.; Li, J.H. Subduction and accretionary tectonics of the East Kunlun orogen, western segment of the Central China Orogenic System. *Earth Sci. Rev.* **2018**, *186*, 231–261. [CrossRef]

22. Huang, H.; Niu, Y.L.; Nowell, G.; Zhao, Z.D.; Yu, X.H.; Zhu, D.C.; Mo, X.X.; Ding, S. Geochemical constraints on the petrogenesis of granitoids in the East Kunlun Orogenic belt, northern Tibetan Plateau: Implications for continental crust growth through syn-collisional felsic magmatism. *Chem. Geol.* **2014**, *370*, 1–18. [CrossRef]

23. Shao, F.L.; Niu, Y.L.; Liu, Y.; Chen, S.; Kong, J.J.; Duan, M. Petrogenesis of Triassic granitoids in the East Kunlun Orogenic Belt, northern Tibetan Plateau and their tectonic implications. *Lithos* **2017**, *282–283*, 33–44. [CrossRef]

24. Xia, R.; Wang, C.M.; Qing, M.; Li, W.L.; Carranza, E.J.M.; Guo, X.D.; Ge, L.S.; Zeng, G.Z. Zircon U–Pb dating, geochemistry and Sr–Nd–Pb–Hf–O isotopes for the Nan'getan granodiorites and mafic microgranular enclaves in the East Kunlun Orogen: Record of closure of the Paleo-Tethys. *Lithos* **2015**, *234–235*, 47–60. [CrossRef]

25. Liang, Y.Y.; Xia, R.; Shan, X.Y.; Ma, Y.; Zhao, E.Q.; Guo, W.H. Geochronology and geochemistry of ore-hosting rhyolitic tuff in the Kengdenongshe polymetallic deposit in the Eastern Segment of the East Kunlun Orogen. *Minerals* **2019**, *9*, 589. [CrossRef]

26. Bian, Q.T.; Li, D.H.; Pospelov, I.; Yin, L.M.; Li, H.S.; Zhao, D.S.; Chang, C.F.; Luo, X.Q.; Gao, S.L.; Astrakhantsev, O. Age, geochemistry and tectonic setting of Buqingshan ophiolites, North Qinghai-Tibet Plateau, China. *J. Asian Earth Sci.* **2004**, *23*, 577–596. [CrossRef]

27. Zhao, X.; Fu, L.B.; Wei, J.H.; Bagas, L.; Santosh, M.; Liu, Y.; Zhang, D.H.; Zhou, H.Z. Late Permian back-arc extension of the eastern Paleo-Tethys Ocean: Evidence from the East Kunlun Orogen, Northern Tibetan Plateau. *Lithos* **2019**, *340–341*, 34–48. [CrossRef]

28. Wang, C.Y.; Zhang, Z.W.; Zhang, C.J.; Chen, C.H.; Li, Y.; Qian, B. Constraints on sulfide saturation by crustal contamination in the Shitoukengde Cu-Ni deposit, East Kunlun orogenic belt, northern Qinghai-Tibet Plateau, China. *Geosci. J.* **2020**, *8*, 356–371. [CrossRef]

29. Guo, X.Z.; Lü, X.B.; Jia, Q.Z.; Li, J.C.; Kong, H.L. Fluid Inclusions and S–Pb Isotopes of the Reshui Porphyry Mo Deposit in East Kunlun, Qinghai Province, China. *Minerals* **2019**, *9*, 547. [CrossRef]

30. Ding, Q.F.; Jiang, S.Y.; Sun, F.Y. Zircon U–Pb geochronology, geochemical and Sr–Nd–Hf isotopic compositions of the Triassic granite and diorite dikes from the Wulonggou mining area in the Eastern Kunlun Orogen, NW China: Petrogenesis and tectonic implications. *Lithos* **2014**, *205*, 266–283. [CrossRef]

31. Liu, Y.J.; Genser, J.; Neubauer, F.; Jin, W.; Ge, X.H.; Handler, R.; Takasu, A. ^{40}Ar/^{39}Ar mineral ages from basement rocks in the Eastern Kunlun Mountains, NW China, and their tectonic implications. *Tectonophysics* **2005**, *398*, 199–224. [CrossRef]

32. He, D.F.; Dong, Y.P.; Liu, X.M.; Yang, Z.; Sun, S.S.; Cheng, B.; Li, W. Tectono-thermal events in East Kunlun, Northern Tibetan Plateau: Evidence from zircon U–Pb geochronology. *Gondwana Res.* **2016**, *30*, 179–190. [CrossRef]

33. Yuan, H.L.; Gao, S.; Dai, M.N.; Zong, C.L.; Günther, D.; Fontaine, G.H.; Liu, X.M.; Diwu, C.R. Simultaneous determinations of U–Pb age, Hf isotopes and trace element compositions of zircon by excimer laser-ablation quadrupole and multiple-collector ICP-MS. *Chem. Geol.* **2008**, *247*, 100–118. [CrossRef]

34. Andersen, T. Correction of common lead in U–Pb analyses that do not report 204Pb. *Chem. Geol.* **2002**, *192*, 59–79. [CrossRef]

35. Liu, Y.S.; Gao, S.; Hu, Z.C.; Gao, C.G.; Zong, K.Q.; Wang, D.B. Continental and oceanic crust recycling-induced melt–peridotite interactions in the Trans-North China Orogen: U–Pb dating, Hf isotopes and trace elements in zircons from mantle xenoliths. *J. Petrol.* **2010**, *51*, 537–571. [CrossRef]

36. Ludwig, K. Mathematical–statistical treatment of data and errors for ^{230}Th/U geochronology. *Rev. Mineral. Geochem.* **2003**, *52*, 631–656. [CrossRef]

37. Wu, F.Y.; Li, X.H.; Zheng, Y.F.; Gao, S. Lu-Hf isotopic systematics and their applications in petrology. *Acta Petrol. Sin.* **2007**, *23*, 185–220. (In Chinese)

38. Zhou, B.; Dong, Y.P.; Zhang, F.F.; Yang, Z.; Sun, S.S.; He, D.F. Geochemistry and zircon U-Pb geochronology of granitoids in the East Kunlun Orogenic Belt, northern Tibetan Plateau: Origin and tectonic implications. *J. Asian Earth Sci.* **2016**, *130*, 265–281. [CrossRef]

39. Li, X.H.; Li, Z.X.; Zhou, H.W.; Liu, Y.; Kinny, P. U-Pb zircon geochronology, geochemistry and Nd isotopic study of Neoproterozoic bimodal volcanic rocks in the Kangdian Rift of South China: Implications for the initial rifting of Rodinia. *Precambrian Res.* **2002**, *113*, 135–154. [CrossRef]

40. Boynton, W.V. Chapter 3—Cosmochemistry of the Rare Earth Elements: Meteorite Studies. *Dev. Geochem.* **1984**, *2*, 63–114.

41. McDonough, W.F.; Sun, S.S. The composition of the Earth. *Chem. Geol.* **1995**, *120*, 223–253. [CrossRef]

42. Blichert, T.J.; Albarède, F. The Lu-Hf isotope geochemistry of chondrites and the evolution of the mantle-crust system. *Earth Planet. Sci. Lett.* **1997**, *148*, 243–258. [CrossRef]

43. Amelin, Y. Meteorite phosphates show constant ^{176}Lu decay rate since 4557 million years ago. *Science* **2005**, *310*, 839–841. [CrossRef] [PubMed]

44. Griffin, W. The Hf isotope composition of cratonic mantle: LAM-MC-ICPMS analysis of zircon megacrysts in kimberlites. *Geochim. Cosmochim. Acta* **2000**, *64*, 133–147. [CrossRef]

45. Campbell, I.H.; Griffiths, R.W. The evolution of the mantle's chemical structure. *Lithos* **1993**, *30*, 389–399. [CrossRef]

46. Macdonald, R.; Rogers, N.; Fitton, J.; Black, S.; Smith, M. Plume-lithosphere interactions in the generation of the basalts of the Kenya Rift, East Africa. *J. Petrol.* **2001**, *42*, 877–900. [CrossRef]

47. Pearce, J. Geochemical fingerprinting of oceanic basalts with applications to ophiolite classification and the search for Archean oceanic crust. *Lithos* **2008**, *100*, 14–48. [CrossRef]

48. Hofmann, A.W. Chemical differentiation of the Earth: The relationship between mantle, continental crust, and oceanic crust. *Earth Planet. Sci. Lett.* **1988**, *90*, 297–314. [CrossRef]

49. Campbell, I.H. Implications of Nb/U, Th/U and Sm/Nd in plume magmas for the relationship between continental and oceanic crust formation and the development of the depleted mantle. *Geochim. Cosmochim. Acta* **2002**, *66*, 1651–1661. [CrossRef]

50. Furman, T.; Bryce, J.; Karson, J.; Iotti, A. East African Rift System (EARS) Plume Structure: Insights from Quaternary Mafic Lavas of Turkana, Kenya. *J. Petrol.* **2004**, *45*, 1069–1088. [CrossRef]

51. Neal, C.R.; Mahoney, J.J.; Chazey, W.J., III. Mantle Sources and the highly variable role of continental lithosphere in basalt petrogenesis of the Kerguelen Plateau and Broken Ridge LIP: Results from ODP Leg 183. *J. Petrol.* **2002**, *43*, 1177–1205. [CrossRef]

52. White, A.; Chappell, B. Granitoid types and their distribution in the Lachlan Fold Belt, Southeastern Australia. *Geol. Soc. Am.* **1983**, *159*, 21–34. [CrossRef]

53. Whalen, J.; Currie, K.; Chappell, B. A-type granites: Geochemical characteristics, discrimination and petrogenesis. *Contrib. Mineral. Petrol.* **1987**, *95*, 407–419. [CrossRef]

54. Sylvester, P. Post-collisional strongly peraluminous granites. *Lithos* **1998**, *45*, 29–44. [CrossRef]

55. Chen, H.W.; Luo, Z.H.; Mo, X.X.; Zhang, X.T.; Wang, J.; Wang, B.Z. SHRIMP ages of Kayakedengtage complex in the East Kunlun Mountains and their geological implications. *Acta Petrol. Mineral.* **2006**, *25*, 25–32.

56. Li, Y.J.; Wei, J.H.; Santosh, M.; Li, H.; Liu, H.W.; Niu, M.W.; Liu, B. Anisian granodiorites and mafic microgranular enclaves in the eastern Kunlun Orogen, NW China: Insights into closure of the eastern Paleo-Tethys. *Geol. J.* **2020**, *55*, 1–21. [CrossRef]

57. Maniar, P.; Piccoli, P. Tectonic discrimination of granitoids. *Geol. Soc. Am. Bull.* **1989**, *101*, 635–643. [CrossRef]

58. Peccerillo, A.; Taylor, S. Geochemistry of Eocene Calc-alkaline volcanic rocks from the Kastamonu Area, Northern Turkey. *Contrib. Mineral. Petrol.* **1976**, *58*, 63–81. [CrossRef]

59. Middlemost, E.A.K. *Magmas and Magmatic Rocks: An Introduction to Igneous Petrology*; Office of Scientific and Technical Information: Oak Ridge, TN, USA, 1986.

60. Meng, F.C.; Zhang, J.X.; Cui, M.H. Discovery of Early Paleozoic eclogite from the East Kunlun, Western China and its tectonic significance. *Gondwana Res.* **2013**, *23*, 825–836. [CrossRef]

61. Li, J.Y.; Qian, Y.; Li, H.R.; Sun, J.L.; Yang, X.M.; Chen, B.; Fan, X.Z. The Late Ordovician granitoids in the East Kunlun Orogenic Belt, Northwestern China: Petrogenesis and constraints for tectonic evolution of the Proto-Tethys Ocean. *Int. J. Earth Sci.* **2019**, *109*, 1439–1461. [CrossRef]

62. Zhou, W.X.; Li, H.Q.; Chang, F.; Lv, X.B. The Early Silurian Gabbro in the Eastern Kunlun Orogenic Belt, Northeast Tibet: Constraints on the Proto-Tethyan ocean closure. *Minerals* **2020**, *10*, 794. [CrossRef]

63. Liu, B.; Ma, C.Q.; Jiang, H.A.; Guo, P.; Zhang, J.Y.; Xiong, F.H. Early Paleozoic tectonic transition from ocean subduction to collisional orogeny in the Eastern Kunlun region: Evidence from Huxiaoqin Mafic rocks. *Acta Petrol. Sin.* **2013**, *29*, 2093–2106. (In Chinese)

64. Dong, G.C.; Luo, M.F.; Mo, X.X.; Zhao, Z.D.; Dong, L.Q.; Yu, X.H.; Wang, X.; Li, X.W.; Huang, X.F.; Liu, Y.B. Petrogenesis and tectonic implications of early Paleozoic granitoids in East Kunlun belt: Evidences from geochronology, geochemistry and isotopes. *Geosci. Front.* **2018**, *9*, 1383–1397. [CrossRef]

65. Wang, G. Metallogenesis of nickel deposits in Eastern Kunlun Orogenic Belt Qinghai Province. Ph.D. Thesis, Jinlin University, Changchun, China, 2014. (In Chinese).

66. Jia, L.H.; Meng, F.C.; Feng, H.B. Eclogite-facies peak fluid activity: Evidence from the British East Kunlun eclogite rock veins. *Acta Petrol. Sin.* **2014**, *30*, 2339–2350. (In Chinese)

67. Pearce, J.A.; Petae, D.W. Tectonic Implications of the Composition of Volcanic ARC Magmas. *Annu. Rev. Earth Planet. Sci.* **1995**, *23*, 251–285. [CrossRef]

68. Kepezhinskas, P.; McDermott, F.; Defant, M.; Hochstaedter, A.; Drummond, M.; Hawkesworth, C.; Koloskov, A.; Maury, R.; Bellon, H. Trace element and SrNdPb isotopic constraints on a three-component model of Kamchatka Arc petrogenesis. *Geochim. Cosmochim. Acta* **1997**, *61*, 577–600. [CrossRef]

69. Chen, J.J.; Fu, L.B.; Wei, J.H.; Selby, D.; Zhang, D.H.; Zhou, H.Z.; Zhao, X.; Liu, Y. Proto-Tethys magmatic evolution along northern Gondwana: Insights from Late Silurian–Middle Devonian A-type magmatism, East Kunlun Orogen, Northern Tibetan Plateau, China. *Lithos* **2020**, *356–357*, 105304. [CrossRef]

70. Liu, B.; Ma, C.Q.; Pan, G.; Zhang, J.Y.; Xiong, F.H.; Jian, H.; Jiang, H.A. Discovery of the Middle Devonian A-type granite from the Eastern Kunlun Orogen and its tectonic implications. *Earth Sci. J. China Univ. Geosci.* **2013**, *38*, 947–962. (In Chinese) [CrossRef]

71. Liu, Y.G.; Lü, X.B.; Ruan, B.X.; Liu, X.; Liu, S.; Jing, F.; Deng, G.; Wang, H.; Zeng, H.D.; Wang, P.; et al. A comprehensive information exploration model for magmatic Cu-Ni sulfide deposits in Beishan, Xinjiang. *Miner. Depos.* **2019**, *38*, 644–666. (In Chinese) [CrossRef]

72. Liu, Y.G.; Li, W.Y.; Lü, X.B.; Liu, Y.R.; Ruan, B.X.; Liu, X. Sulfide saturation mechanism of the poyi magmatic Cu-Ni sulfide deposit in Beishan, Xinjiang, Northwest China. *Ore Geol. Rev.* **2017**, *91*, 419–431. [CrossRef]

73. Liu, Y.G.; Wang, L.P.; Mei, S.H.; Li, W.Y.; Kohlstedt, D.L.; Zhang, Z.W. Experimental discrimination of typical "benificail crustal contamination" and "harmful crustal contamination" during the sulfide saturation process of magmatic Cu-Ni-PGE deposit. In Proceedings of the 9th National Symposium on Mineralization Theory and Prospecting Methods, Nanjing, China, 13–16 December 2019; Volume 78. (In Chinese)